energies

MDPI

Article

Enhance of Energy Harvesting from Transverse Galloping by Actively Rotating the Galloping Body

Antonio Barrero-Gil *, David Vicente-Ludlam, David Gutierrez and Francisco Sastre

School of Aeronautics, Plaza Cardenal Cisneros 3, Technical University of Madrid, 28040 Madrid, Spain; david.vicente@upm.es (D.V.-L.); david.gutierrezg@alumnos.upm.es (D.G.); francisco.sastre@upm.es (F.S.)
* Correspondence: antonio.barrero@upm.es

Received: 16 October 2019; Accepted: 12 December 2019; Published: 23 December 2019



Abstract: Kinematic rotary control is here proposed conceptually to enhance energy harvesting from Transverse Galloping. The effect of actively orientating the galloping body with respect to the incident flow, by imposing externally a rotation of the body proportional to the motion-induced angle of attack, is studied. To this end, a theoretical model is developed and analyzed, and numerical computations employing the Lattice Boltzmann Method are carried out. Good agreement is found between theoretical model predictions and numerical simulations results. It is found that it is possible to increase significantly the efficiency of energy harvesting with respect to the case without active rotation, which opens the path to consider this idea in practical realizations.

Keywords: galloping; energy harvesting; active control

1. Introduction

During the last decade, the applied interest in the field of Flow-Induced vibrations has been enlarged by considering phenomena like Transverse Galloping or Vortex-induced Vibrations as the means to harvest useful energy from fluid flows. In those cases, the aim is to promote the Flow-Induced vibration phenomenon, in order to extract as much as possible part of the kinetic energy from the incoming flow and to transfer it to the body, in the form of mechanical oscillatory energy, and subsequently convert this mechanical energy into electrical energy by electromagnetic, piezoelectric, or electrostatic means. Bernitsas and his group of collaborators [1,2] proposed a system for electric power generation from marine/river currents taking advantage of the phenomenon of oscillations induced by vortex detachment in cylinders (Vortex-Induced Vibrations). Later on, in [3], the idea of taking advantage of the Transverse Galloping phenomenon was considered and, through analytical modeling, the role of the main parameters governing the problem, namely the geometry of the cross-section, mechanical parameters (mass, damping, stiffness) and flow velocity, was established and high energy transfer potential was proven. Since then, different concepts of energy extraction based on Transverse Galloping have appeared, with a focus on the large scale where a significant production of electric energy is desired [4], or to generate small amounts of electrical energy (of the order of milli-Watts) that can be used, for example, to supply electrical power to autonomous sensors and actuators and to avoid their dependence on batteries; see, for example, [5–9].

Very briefly, we can say that Transverse Galloping is a fluid-elastic instability that appears in some elastic bluff bodies when the velocity of the incident flow exceeds a critical value. Then, a small transverse displacement of the body induces an angle of attack relative to the incoming flow and a fluid force appears in the direction of the displacement in such a way that a net flux of energy from the fluid flow to the body appears and the later starts to oscillate transverse to the flow with increasing amplitude until a Limit Cycle of Oscillations is reached. Transverse Galloping is a self-induced phenomenon mainly driven by the motion-induced angle of attack (and not by vortex shedding

like in Vortex-Induced Vibrations), which can only appear for specific cross-sections in which a variation of the motion-induced angle of attack produces a transverse fluid force in the direction of the velocity of oscillation. One notable difference of Transverse Galloping response compared to that of Vortex-Induced Vibrations is that, in the former, the amplitude of oscillations grows continuously with the incoming flow speed limit. For a detailed review of Transverse Galloping characteristics, the reader is referred to [10–12].

In a simplified manner, an energy-focused Transverse Galloping system is comprised of three main elements: (i) the galloping body, immersed in the fluid flow where the transverse fluid forces appear responsible for the transverse galloping phenomenon, (ii) the elastic system provides the restoring force and allows oscillations to happen, and (iii) a transducer, where the oscillatory mechanical power of the body is converted into electrical energy. The problem is fully coupled (double coupling fluid-solid-electrical), thus an integral perspective has to be taken into account in order to fully establish design rules to be able to harness energy efficiently. Some optimization studies in these three different elements have been carried out in the past: for example [3,13], looking for optimal cross-section geometry of the galloping body (let us say, looking for optimization on the "fluid side"); Reference [14] focused on the optimization of the "elastic side" by considering a dual mass system, or [15,16] working in the "electrical side", looking for the optimal electrical impedance.

Here, we present a forward step in the search for optimal solutions from the "fluid side" (that is, fluid–solid interaction) part of the energy-focused galloping system, and we study the effect of actively orientating the galloping body with respect to the incident flow by imposing externally a rotation of the body. In combination with the vertical motion, the rotation contributes to change the angle of attack of the body with respect to the incoming flow and hence the flow around it and the transverse fluid force and, therefore, the energy transfer from the flow to the oscillating body. Questions naturally arising are, for example, *How does it affect rotation?*, *Can more power be harnessed?*, *Which is the optimal rotation law?* In order to shed light on these questions, a theoretical model, where quasi-steady hypothesis is taken into account, to include the effect of the rotation has been developed and presented here. Since transverse galloping is driven by the motion-induced angle of attack, which is linked to the velocity of body oscillations, here we consider that rotation is proportional to the motion-induced angle of attack. As will be shown, following this strategy, the energy transfer from the flow to the galloping body can be significantly increased.

In the following section, Section 2, the theoretical model developed is presented and analyzed. A validation of the model is carried out in Section 3 by comparison with results obtained via numerical simulations following the Lattice Boltzmann Method. Finally, concluding remarks are drawn in Section 4.

2. Theoretical Model

For modeling purposes, we consider the simplified case of a prismatic galloping body elastically mounted in such a way that oscillations take place only on the transverse direction of the flow and is actively forced to rotate along its longitudinal axis with a prescribed rotation law (see Figure 1). The body is linked to a harvester system in order to extract useful energy. For simplicity, a generic linear viscous damper is considered here to model the harvester system. This can be a good approximation, for example, for electromagnetic conversion when the frequency of oscillations is low so that the effect of the inductance is negligible. In this case, the mechanical effect of the harvester is equivalent to that of a viscous damper, as shown briefly in the Appendix B or in [15,17]. Note that only energy is harvested from the transverse motion. Appropriate balance between inertia, stiffness, backlash force from the harvester, and fluid force gives the following ordinary differential equation for the transverse displacement y:

$$m\ddot{y} + c\dot{y} + ky = \frac{1}{2}\rho U^2 D C_Y, \tag{1}$$

where m is the mass per unit length of the body, c is a damping constant per unit length due to the harvester (note that $-c\dot{y}$ is the backlash force due to the harvester), k is the stiffness constant per unit length, ρ is the fluid density, U is the undisturbed velocity of the incident flow, D the cross-section length of the body, and C_Y is the instantaneous fluid force coefficient in the transverse direction to the incident flow. Finally, the dot symbol stands for differentiation with respect to physical time t.

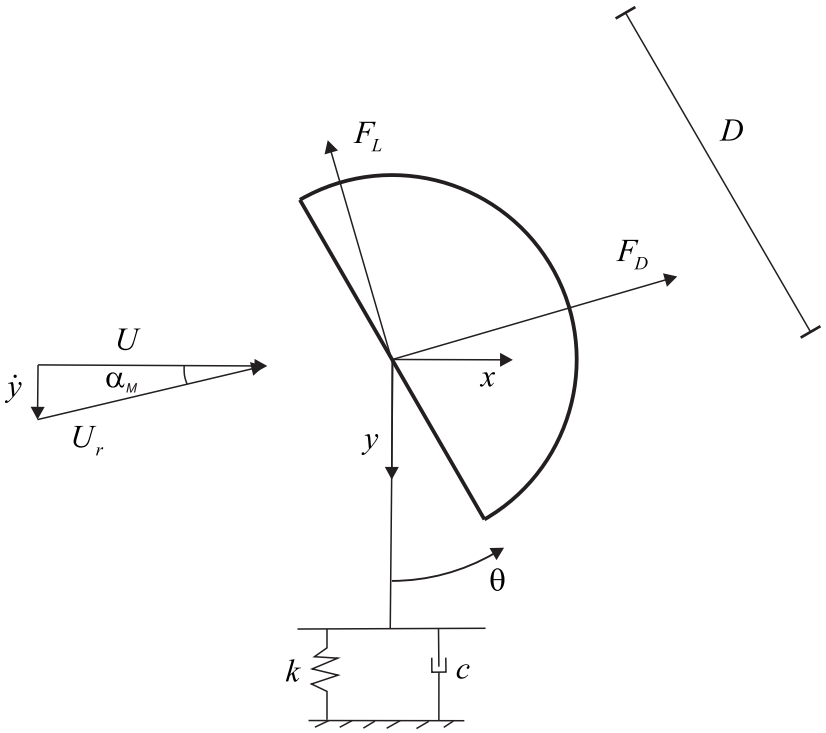


Figure 1. Schematics of the forces acting on the galloping body.

Equation (1) can now be rewritten in dimensionless form taking D and $\omega_N^{-1} = (m/k)^{1/2}$ as characteristic lengthscale and timescale. Then,

$$Y'' + 2\zeta Y' + Y = \frac{U^{*2}}{2m^*} C_Y, \tag{2}$$

where a comma stands differentiation with respect to the dimensionless time, $\tau = \omega_N t$, $Y = y/D$ is the normalized displacement, $\zeta = c/(2m\omega_N)$ is the dimensionless damping, $U^* = U/(\omega_N D)$ the reduced velocity, and $m^* = m/(\rho D^2)$ is the mass ratio.

In order to describe C_Y, the quasi-steady hypothesis is usually resorted to [12] since galloping is typically a low-frequency oscillation phenomenon where the characteristic timescale of the oscillation (of order $2\pi(m/k)^{1/2}$) is large enough compared to the characteristic timescale of the flow (of order D/U). Then, the fluid force is only dependent on the instantaneous attitude of the prism with respect to the incident flow, and can be evaluated through the steady drag and lift fluid force coefficients evaluated at the instantaneous angle of attack. In this case, due to the rotation of the body, the angle of attack α is the sum of the motion-induced angle of attack α_M and the rotation applied to the body θ that is $\alpha = \alpha_M + \theta$, see Figure 1, and therefore

$$C_Y = \left(\frac{U_r}{U}\right)^2 \left(-C_L\left(\alpha_M + \theta\right)\cos\alpha_M - C_D\left(\alpha_M + \theta\right)\sin\alpha_M\right). \tag{3}$$

Since $\cos\alpha_M = U/U_r$, it follows that

$$C_Y = -\frac{1}{\cos\alpha_M}\left(C_L\left(\alpha_M+\theta\right)+C_D\left(\alpha_M+\theta\right)\tan\alpha_M\right). \tag{4}$$

From Figure 1, it follows that $\tan\alpha_M = \dot{y}/U = Y'/U^*$ so that, in a generic sense, if θ is known at any instant (rotating law) as well as lift and drag coefficients, C_L and C_D, dependence with angle of attack, Equation (2) may be solved taking into account Equation (4).

Here, in order to go forward in the analytical modeling of the problem, maintaining a compromise between simplicity, to make a useful comprehensive analysis, and accuracy, let us approximate the C_L and C_D dependence with angle of attack by just two-term polynomial functions,

$$C_L \approx l_1\alpha + l_3\alpha^3, C_D \approx d_0 + d_2\alpha^2, \tag{5}$$

where l_1, l_3, d_0, d_2 are fitting coefficients that depend mainly on the cross-section geometry and Reynolds number. An odd polynomial has been considered for C_L and an even one for C_D because the cross-section of galloping bodies present usually symmetry with respect to the direction at zero angle of attack [10].

Substituting Equation (5) into Equation (4) gives

$$C_Y \approx -\frac{1}{\cos\alpha_M}\left(l_1(\alpha_M+\theta)+l_3(\alpha_M+\theta)^3+\left(d_0+d_2(\alpha_M+\theta)^2\right)\tan\alpha_M\right), \tag{6}$$

which, for a fixed cross-section and Reynolds number, expresses the vertical fluid force coefficient as a function of the motion-induced angle of attack (α_M) and rotation law (θ).

2.1. Rotation Proportional to the Motion-Induced Angle of Attack

As anticipated earlier, galloping is driven by the motion-induced angle of attack, so that it seems natural to consider a rotation law proportional to the motion-induced angle of attack. Therefore, we consider the case where the galloping body is rotated as

$$\theta = K_1\alpha_M, \tag{7}$$

where K_1 is a constant of proportionality. Substituting Equation (7) into Equation (6), one finds

$$C_Y = -\frac{1}{\cos\alpha_M}\left(l_1(1+K_1)\alpha_M+l_3(1+K_1)^3\alpha_M^3+\left(d_0+d_2(1+K_1)^2\alpha_M^2\right)\tan\alpha_M\right), \tag{8}$$

so that C_Y is now a function of α_M for each value K_1. The motion-induced angle of attack is small if the velocity of oscillation is small compared to the incoming flow speed, since $\alpha_M = \tan^{-1}(Y'/U^*)$. In those cases, we can make $\alpha_M \approx \tan\alpha_M$, $\cos\alpha_M \approx 1$ and therefore from Equation (8),

$$C_Y = -\left(\left(l_1\left(1+K_1\right)+d_0\right)\right)\tan\alpha_M - \left(d_2\left(1+K_1\right)^2+l_3\left(1+K_1\right)^3\right)\tan\alpha_M^3, \tag{9}$$

or written in a more compact way,

$$C_Y = \tilde{a_1}\tan\alpha_M + \tilde{a_3}\tan\alpha_M^3, \tag{10}$$

with

$$\tilde{a_1} = -l_1(1+K_1) - d_0, \tag{11}$$

and

$$\tilde{a_3} = -d_2(1+K_1)^2 - l_3(1+K_1)^3. \tag{12}$$

In Equation (10), the galloping aerodynamics is given by two coefficients where the rotation effect is included. This notation is convenient in order to make easy comparison with energy harvesting

results obtained previously for the case without rotation [3]. Substituting Equation (10) into Equation (2) and taking into account that $\tan\alpha_M = Y'/U^*$, one finds

$$Y'' + 2\zeta Y' + Y = \frac{U^{*2}}{2m^*}\left(\tilde{a_1}\frac{Y'}{U^*} + \tilde{a_3}\frac{Y'^3}{U^{*3}}\right). \tag{13}$$

For galloping, it is necessary that $\tilde{a_1} > 0$ (that is $-l_1(1+K_1) - d_0 > 0$), and then $\tilde{a_3} < 0$.

It is instructive to see how K_1 affects galloping coefficients, and it can be seen that

$$\frac{\tilde{a_1}}{a_1} = 1 + \frac{1}{1+c_1}K_1, \tag{14}$$

where $c_1 = d_0/l_1$. This shows that $\tilde{a_1}/a_1$ is linearly proportional to K_1 (note a_1 is the first (linear) galloping coefficient without actuation that is $a_1 = \tilde{a_1}$ for $K_1 = 0$). d_0 is positive (drag coefficient at angle of attack zero) and for galloping bodies $l_1 < 0$, so the first galloping coefficient will be increased for positive values of K_1.

In addition, we can find

$$\frac{\tilde{a_3}}{a_3} = \frac{1}{1+c_2}(1+K_1)^2 + \frac{c_2}{1+c_2}(1+K_1)^3, \tag{15}$$

where $a_3 = -d_2 - l_3$ is the nonlinear galloping coefficient without actuation ($K_1 = 0$) and $c_2 = l_3/d_2$. Note that, for galloping bodies, $a_1 = -d_0 - l_1 > 0$ so that $-1 < c_1 < 0$ and $a_3 = -d_2 - l_3 > 0$, which means that $c_2 < -1$.

2.2. Galloping Response

Equation (13) allows an analytical approach when the nonlinear terms are small compared to the linear ones—that is, when $m^*U^* \gg 1$. In this case, solution to the nonlinear Equation (13) is close to that of its linear version and thus one may assume that the steady-state response is sinusoidal, $Y = A^*\sin(\omega^*\tau)$, where $A^* = A/D$ and $\omega^* = \omega/\omega_N$ being A and ω the amplitude circular frequency of steady-state oscillations. In addition, if one takes into account that $\cos^3(\omega^*\tau) \approx 3\cos(\omega^*\tau)/4$, (i.e., higher order terms in $\cos(3\omega^*\tau)$ are neglected), equating sine and cosine terms, after some algebra, one gets

$$\omega^* = 1; \qquad A^* = \left(\frac{4U^*}{3\tilde{a_3}}\left(4m^*\zeta - \tilde{a_1}U^*\right)\right)^{1/2}. \tag{16}$$

Oscillations are only possible when $A^* > 0$, thus the initial reduced velocity at which galloping oscillations are expected is recovered $U_g^* = 4m^*\zeta/\tilde{a_1}$. As $\tilde{a_1}$ increases for larger values of K_1 (see Equation (14)), the initial reduced velocity where galloping starts is reduced as K_1 is increased. Noteworthy, for high enough negative values of K_1, $\tilde{a_1}$ takes a negative value and galloping is avoided, which are interesting results from the practical side when the interest is to protect a structural element against Transverse Galloping.

An important parameter is the asymptotic slope of A^* for large enough U^*, obtained by considering $4m^*\zeta$ to be much smaller than $\tilde{a_1}U^*$, which yields

$$\frac{A_\infty^*}{U^*} = \left(-\frac{4\tilde{a_1}}{3\tilde{a_3}}\right)^{1/2}. \tag{17}$$

2.3. Energy Harvesting Efficiency

The net mean power harvested is the mean power harnessed P_H at the viscous damper minus the losses due to the power spent to rotate the prism. The mean power applied to rotate the prism P_R is

$$P_R = \frac{1}{T}\int_0^T (T_I + T_F)\dot{\theta} dt, \tag{18}$$

where T_I refers to the inertial torque, T_F is the fluid torque on the body, and T is an averaging time. T_I is proportional to the angular acceleration $\ddot{\theta}$, thus, for close-to-sinusoidal actuation, the contribution to Equation (18) is negligible. In addition, T_F in a quasi-steady manner is proportional to the angular position θ; hence, for near sinusoidal rotations, these terms can also be neglected, resulting in an overall null power consumption.

The mean power harnessed P_H at the viscous damper can be defined as

$$P_H = \frac{1}{T}\int_0^T c\dot{y}^2 dt. \tag{19}$$

For sinusoidal oscillations of amplitude A and circular frequency ω, $y(t) = A\sin(\omega t)$ and $\dot{y} = A\omega\cos(\omega t)$. Substituting $\dot{y}$ into Equation (19), it follows that

$$P_H = \frac{cA^2\omega^2}{2} = m\omega_N^3 D^2 \zeta A^{*2}\omega^{*2}. \tag{20}$$

A conversion factor (or efficiency) can be introduced in the same way as in [3], as the mean power dissipated at the viscous damper divided by the total power in the incoming flow per unit length,

$$\eta = \frac{P_H}{\frac{1}{2}\rho U^3 D}. \tag{21}$$

Substituting Equation (16) into Equations (20) and (21), one finds

$$\eta = \frac{8m^*\zeta}{3\tilde{a_3}U^{*2}}\left(4m^*\zeta - \tilde{a_1}U^*\right). \tag{22}$$

The maximum efficiency can be found by differentiating Equation (22) with respect to U^* and equating to zero:

$$\eta_{max} = \frac{-\tilde{a_1}^2}{6\tilde{a_3}}, \tag{23}$$

which happens at a reduced velocity of $U^* = 2U_g^*$.

It is instructive to compare the maximum efficiency with actuation to that achieved without actuation ($K_1 = 0$). To this end, let us substitute Equations (14) and (15) into Equation (23),

$$\eta_{max} = \frac{-\tilde{a_1}^2}{6\tilde{a_3}} = -\frac{a_1^2}{6a_3}\frac{\left(1+\frac{K_1}{1+c_1}\right)^2}{\frac{(1+K_1)^2}{1+c_2} + \frac{c_2(1+K_1)^3}{1+c_2}} = \eta_{max0}M, \tag{24}$$

where $\eta_{max0} = -a_1^2/(6a_3)$ is the maximum efficiency achieved without actuation and M is a function of K_1 and cross-section aerodynamic characteristics (c_1 and c_2 or, equivalently, d_0/l_1 and l_3/d_2) that recovers the rotation effect in maximum efficiency. When $M > 1$, rotation enhances energy harvesting efficiency. For positive values of K_1, from Equation (24), it is seen that M is greater than one if

$$c_2 < \frac{-2c_1^2 - 2c_1}{3c_1^2 + 4c_1 + 1}. \tag{25}$$

Figure 2 shows graphically the zone of aerodynamic parameters $d_0/l1$ and l_3/d_2 where positive actuation ($K_1 > 0$) means an increase in maximum efficiency (that is, $M > 1$).

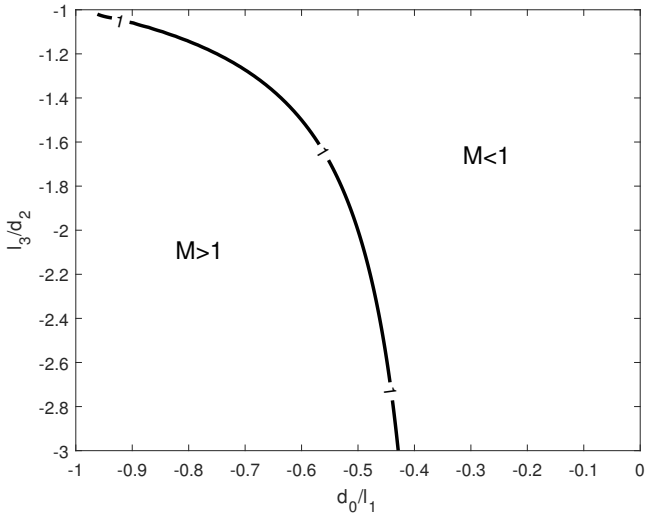


Figure 2. Boundary of magnification factor equal to one, $M = 1$, as a function of $c_1 = d_0/l_1$ and $c_2 = l_3/d_2$.

It is also possible to compute the optimal value of K_1 by differentiating Equation (24) with respect to K_1, equating to zero and solving, to get

$$K_1^{op} = -\left(1 + C + 3c_1/2\right), \tag{26}$$

with

$$C = \left(c_1\left(9c_1c_2 - 8\right)/c_2\right)^{1/2}. \tag{27}$$

Then, the maximum magnification of efficiency with actuation is obtained by evaluating (see Equation (24)) at K_1^{op} giving the

$$M_{max} = -\frac{2(2C + c_1)^2(c_2 + 1)}{(2C + 3c_1)^2(c1 + 1)^2(2C + 3c_1c_2 - 2)}, \tag{28}$$

a relationship that is shown graphically in Figure 3. As seen, magnification due to actuation grows as both c_1 and c_2 grows (in absolute value).

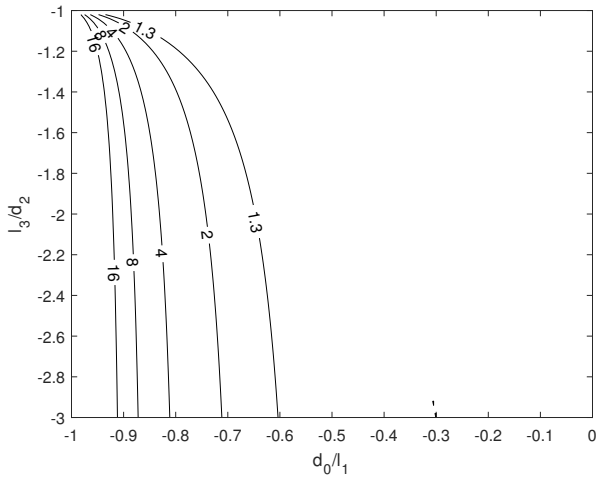


Figure 3. Contour plot of maximum magnification factor M_{max} as a function of $c_1 = d_0/l_1$ and $c_2 = l_3/d_2$.

3. Numerical Simulations and Validation of the Mathematical Model

In order to validate the mathematical model presented earlier and check the results it provided, we carried out numerical simulations of the fluid–structure interaction problem at hand using a previously validated Lattice Boltzmann Method code (see [18] or Appendix A for details). The problem sketched in Figure 1 was solved numerically where a D-section galloping body was taken into account. A D-section has been chosen following the work presented in [19], where several cross-section shapes were analyzed (triangles, biconvex, rhombi, and D-shape). It was shown that, for energy extraction purposes, the most suitable shape is the D-section. The transverse dynamics of the body are governed by Equation (2), and the body is forced to rotate around the center point ($x = 0, y = 0$) following the law given in Equation (7). The instantaneous fluid force coefficient C_Y is now computed with the Lattice Boltzmann Method (instead of analytically taking into account the quasi-steady hypothesis, as made in Section 2). The mass ratio m^* of the body was 10, mechanical damping $\zeta = 0.04$, the Reynolds number 100, and the natural frequency of oscillations was varied to change the reduced velocity U^* in each simulation case. The Reynolds number was 100 in order to have a reasonable computational cost that allows for solving a large number of cases in an affordable time. For each simulation case, the temporal evolution of the flow field, temporal evolution of displacement of the D-section cylinder, and fluid forces and torque on it are found. Then, the steady-state of oscillations is obtained (say A^* and ω^*; in all cases, oscillations were sinusoidal) as well as mean power dissipated at the harvester and mean power spent to rotate the cylinder.

3.1. Computational Domain and Boundary Conditions

The computational domain and boundary conditions are shown in Figure 4. The diameter of the D-Section has 40 lattice points (observe that the number of lattice points for the diameter of the cylinder N_D is linked to the Reynolds number Re, kinematic viscosity ν, and inflow velocity U (free of turbulence), since $N_D = \nu Re/U$) and the computational domain chosen is 40D × 30D, giving a size of 1600 × 1200 lattice points. The left boundary was set to be a velocity specified inflow boundary condition with constant velocity profile U. To simulate the incompressible condition, the Mach number must be low enough; to this end, the inflow velocity U was set to 0.05 (the velocity of sound is $c_s = 1/\sqrt{3}$ so that the Mach number at the inflow is $Ma = U\sqrt{3}$ and Ma^2 is of order 0.01). The rest of the outer computational boundaries were considered outflows. For the boundary conditions on the body, a no-slip boundary condition has been applied that is fluid velocity equal to body velocity (see Appendix A for details about how physical boundary conditions are implemented).

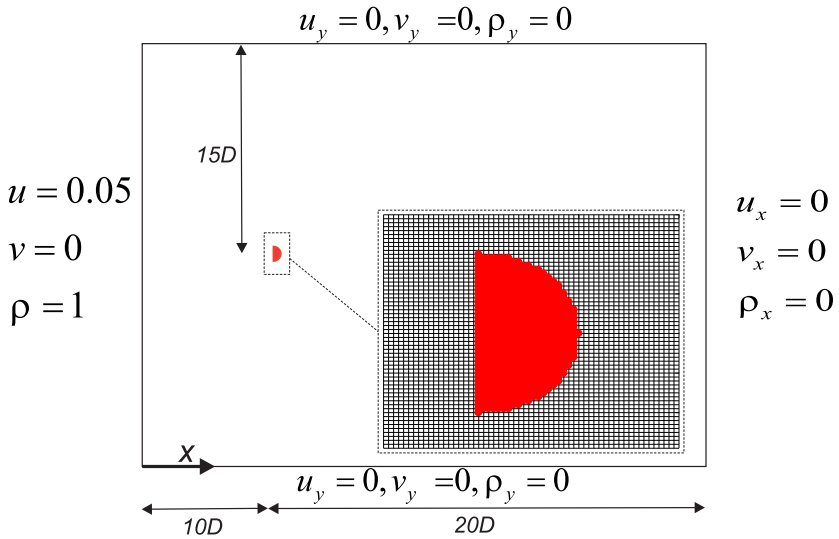


Figure 4. Schematics of the computational domain and boundary conditions. Detailed mesh around the cross-section is also shown.

3.2. Results

First of all, static numerical simulations were carried out to compute static drag and lift coefficients. To this end, no-motion was imposed ($Y = Y' = Y'' = 0$) and a fixed angle of attack (θ fixed). Figure 5 shows the dependence of the lift and drag coefficients with the angle of attack α from the numerical simulations carried. As said before, the Reynolds number was 100. In addition, results from [20] are presented for validation purposes, as well as polynomial fitting curves obtained by least squares minimization (see Equation (5); $l_1 = -2.28, l_3 = 1.44$, $d_0 = 2.05$ and $d_2 = -1.20$).

In Figure 6left, the theoretical variation of galloping coefficients $\tilde{a_1}$ and $\tilde{a_3}$ with K_1 is shown. Note that this variation is obtained from Equations (11) and (12) once fitting coefficients for C_L and C_D are known. Figure 6right shows the transverse fluid force coefficient C_Y as a function of the motion induced angle of attack α_M, for different values of K_1 (see Equation (9)). It can be seen that, as K_1 is increased so is the maximum value of C_Y, but such maximum occurs for lower values of α_M. In addition, increasing K_1 makes the curve of C_Y with respect to α_M narrower and the cut of the curve with $C_Y = 0$ occurs for lower values of α_M, except for a small range between $0 < K_1 < 0.3$.

Figure 7 presents steady-state amplitude of oscillations and energy harvesting efficiency as a function of the the reduced velocity for two different positive values of K_1. As can be seen, the quasi-steady theoretical model presented (Equation (16)) for the normalized amplitude of oscillations and Equation (22) for the efficiency) is capable of predicting fairly correctly the amplitude of oscillation and, to a lesser extent, the efficiency of energy harvesting when compared to the full fluid–structure–interaction numerical simulations which also showed a nearly sinusoidal response. For $K_1 = 0.5$, the maximum efficiency achieved is 0.14 (taken from numerical computations), whereas, for $K_1 = 1$, this figure has been increased to 0.16.

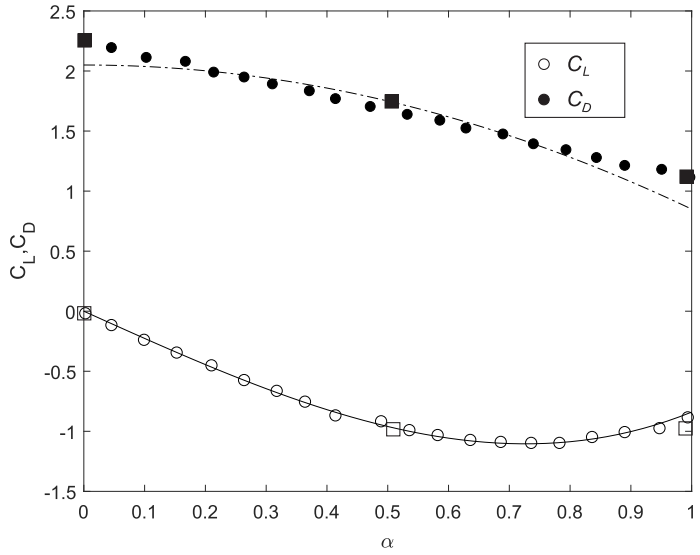


Figure 5. C_L and C_D static coefficients dependence on the angle of attack (in radians) computed through numerical Lattice Boltzmann Method computations for a D-section at Re = 100. Polynomial fitting is shown with a solid line for C_L ($l_1 = -2.28, l_3 = 1.44$) and dashed line C_D ($d_0 = 2.05$ and $d_2 = -1.20$) for For comparison purposes, results (squares) from [20] are also presented.

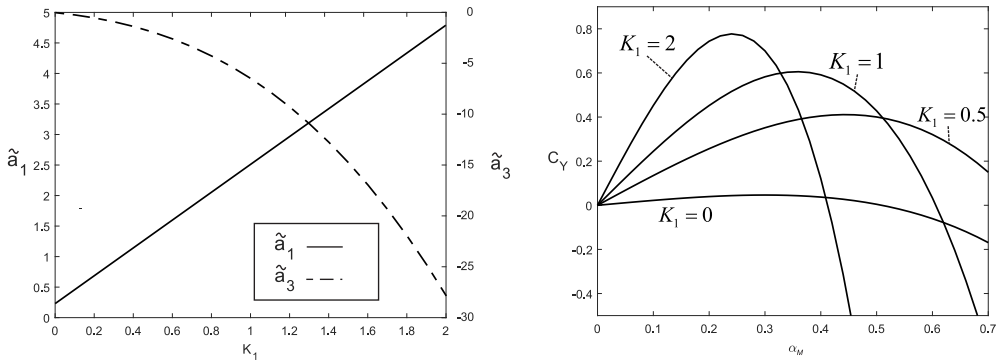


Figure 6. (**left**) Variation of $\tilde{a_1}$ and $\tilde{a_3}$ with K_1. (**right**) Transverse fluid force coefficient C_Y as a function of the motion induced angle of attack α_M for different positive values of K_1.

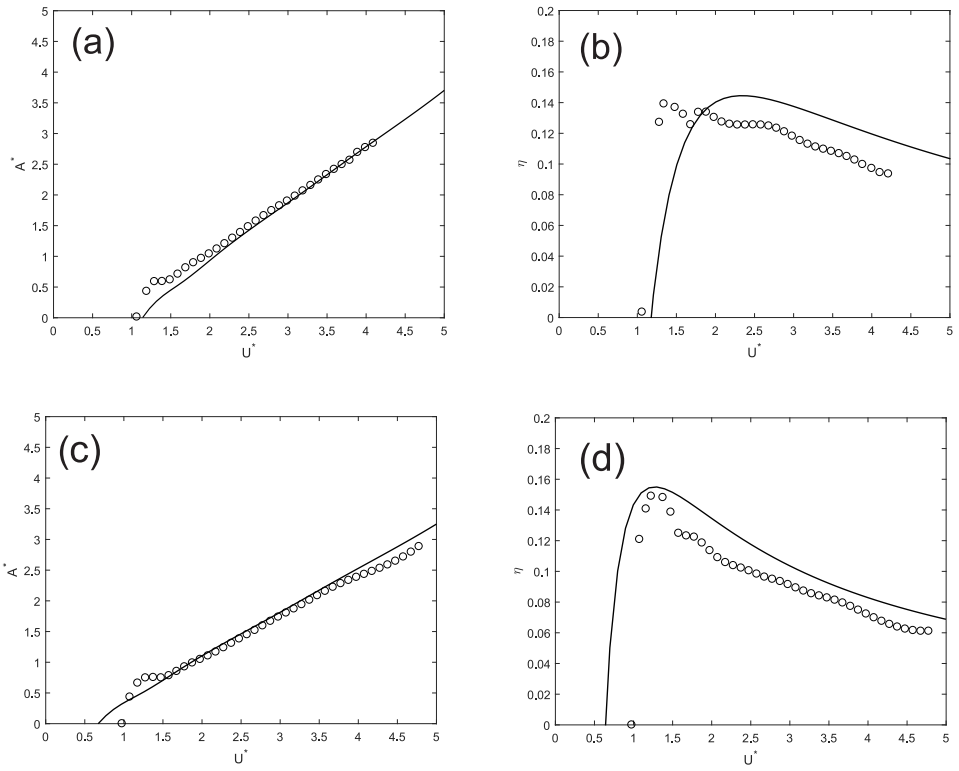


Figure 7. Normalized amplitude of oscillations A^* and efficiency η as function of the reduced velocity U^* for $K_1 = 0.5$ (**a**,**b**) and $K_1 = 1$ (**c**,**d**). White circles stand for results from the Lattice Boltzmann Method computations and solid lines from the quasi-steady model.

Figure 8 plots the maximum efficiency η_{max} as a function of K_1 predicted by the theoretical model (Equation (24)) along with results obtained in numerical simulations. Agreement between theoretical model and computational results is good. Regarding computational results, for $K_1 = 0$, galloping solution without rotation, the maximum efficiency is $\eta_{max0} = 0.05$. As K_1 is increased, the efficiency increases rapidly with K_1 until a maximum efficiency of $\eta_{max} = 0.16$, obtained at $K_1 = 0.8$. Further increasing K_1 leads to a slow reduction of the maximum efficiency achievable. Therefore, through the rotation law investigated (and for a D-section at Reynolds 100), it is possible to increase the maximum achievable efficiency by a factor slightly higher than three times. It is noteworthy that the low efficiency for $K_1 = 0$ is mainly due to the Reynolds number (as it has a major effect on the detachment of the flow) and thus it is expected that, for the D-section at higher Reynolds number (or another cross-section shape), the maximum efficiency at $K_1 = 0$ will be higher and thus there will be a potential to obtain high values of η_{max} thought the rotation actuation proposed.

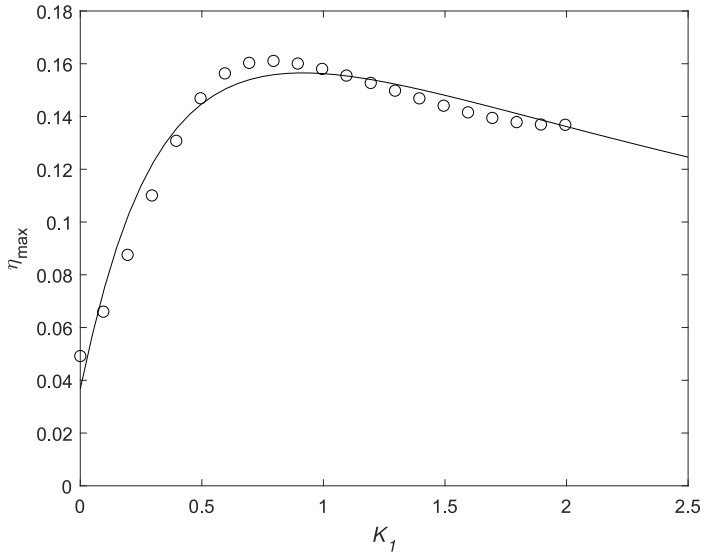


Figure 8. Maximum efficiency of energy harvesting as a function of K_1. Results from Lattice Boltzmann Method computations are in white circles and theoretical predictions are from the quasi-steady model (Equation (24)).

It is interesting to study how much power is spent to rotate the body in order to see to what extent the hypothesis introduced in the theoretical model (that is, zero mean power to rotate the body) is valid. The mean power to rotate the body is:

$$P_R = \frac{1}{T}\int_0^T \left(M + \frac{1}{8}mD^2\ddot{\theta}\right)\dot{\theta}dt, \tag{29}$$

where T is an averaging time, M the fluid torque applied on the center of rotation, and $\dot{\theta}$ and $\ddot{\theta}$, respectively, the rotation velocity and acceleration.

Equation (29) can be made dimensionless dividing it by the kinetic power in the incoming flow:

$$\eta_R = \frac{2P_R}{\rho U^3 D}. \tag{30}$$

As an example, for a reduced velocity of $U^* = 2.75$ and $K_1 = 0.5$, a value of $\eta_R = -0.0013$ was computed, whereas the efficiency of energy harvesting is 0.125, meaning that the power spent to rotate the body is around 1% of the power harvester. This result corroborates the idea taken from the quasi-steady analysis: the power spent to rotate the body should be small. Figure 9 shows numerical results obtained for $U^* = 2.75$ and $K_1 = 0.5$, in terms of dimensionless amplitude of transverse oscillations (Figure 9a), fluid torque coefficient (Figure 9b), velocity of rotation and acceleration of rotations (Figure 9c). The following can be observed: (i) the transverse oscillations are quasi-sinusoidal, (ii) velocity and acceleration of rotating angle are nearly sinusoidal and there is almost a 90º phase shift between them so that the contribution to Equation (29) is nearly zero, and (iii) the torque is close to being in phase with rotation angle. These results explain that power spent to rotate the body is small.

For a better understanding from the physical point of view, the flow pattern (vorticity) around the galloping body is presented here for the case without actuation ($K_1 = 0$) and for a particular case with actuation ($K_1 = 1$), reduced velocity 4 and $\zeta = 0.04$. In Figure 10, the wake structure after the body without actuation exhibits characteristic large-scale vortices being shed independently from the body's oscillation at its own frequency. Thus, the wake pattern resembles that of a wave as each vortex is shed at different points of the cycle of oscillation following the Strouhal frequency of vortex emission for the body at rest ($f_v/f_N = StU^*$, where St is the characteristic Strouhal number of the cross-section

and f_v the frequency of vortex shedding); thus, there is no synchronization between vortex shedding and oscillation.

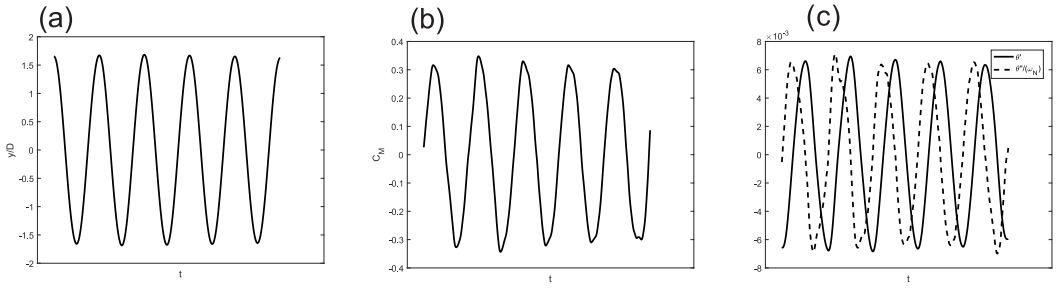


Figure 9. (**a**) temporal evolution of the dimensionless transverse displacement of the body; (**b**) fluid torque coefficient evolution in time; (**c**) rotation speed and acceleration. $U^* = 2.75$, $K_1 = 0.5$, $m^* = 10$, $\zeta = 0.04$, where a steady-state of oscillations has been reached.

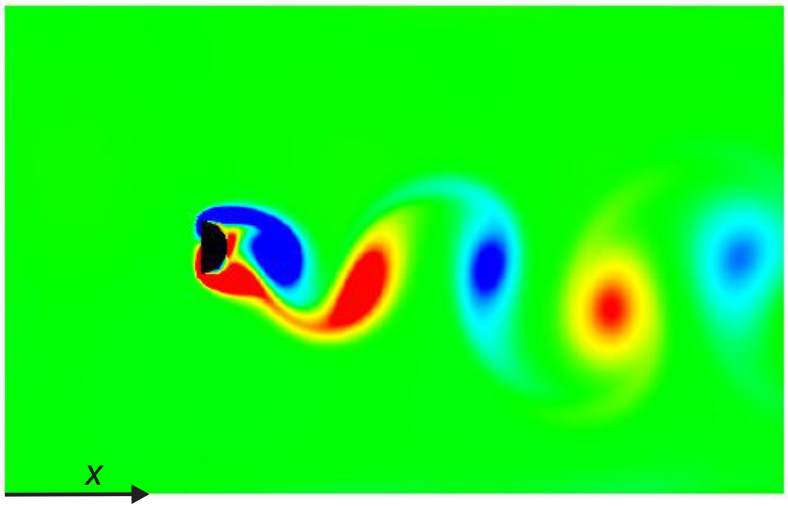


Figure 10. Vorticity contour without actuation for a reduced velocity of $U^* = 4$, mass ratio m^* is 10, and damping parameter $\zeta = 0.04$. The vorticity field when the body is at $Y = 0$ and going upwards is shown.

On the other hand, in Figure 11, the wake after the body with actuation ($K_1 = 1$) exhibits a quite different flow pattern. Only independent vortices are formed at the point of maximum displacement during the cycle of oscillations when the body changes direction (maximum acceleration). The near-wake behind the body shows bounded vorticity which only breaks into an independent vortex downstream. This could be related to the fact that, through orientating the galloping body, it becomes much less bluff and the flow remains further attached.

For completeness, other cross-section shapes (equilateral triangle, rectangle and 45º rhombi) have been numerically simulated for $U^* = 4$, $K_1 = 1$ (also $m* = 10$ and $\zeta = 0.04$). In terms of energy extraction efficiency, the following figures were obtained: $\eta = 0.09$ for the D-shape, $\eta = 0.04$ for the equilateral triangle, $\eta = 0.01$ for the rectangular body (1:2 side relationship), and $\eta = 0.001$ for the rhombus. From Figures 11 and 12, it is seen that the most slender near-wake is given for the D-shape one.

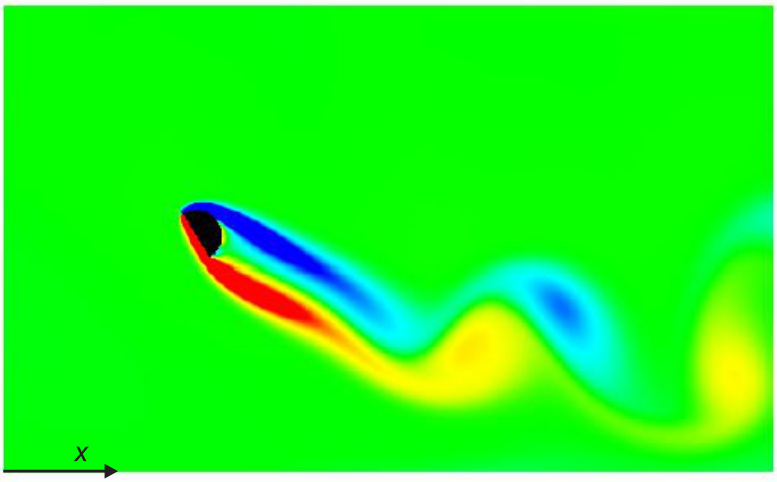


Figure 11. Vorticity contour with actuation ($K_1 = 1$) for a reduced velocity of $U^* = 4$, mass ratio m^* is 10, and damping parameter $\zeta = 0.04$. The vorticity field when the body is at $Y = 0$ and going downwards is shown.

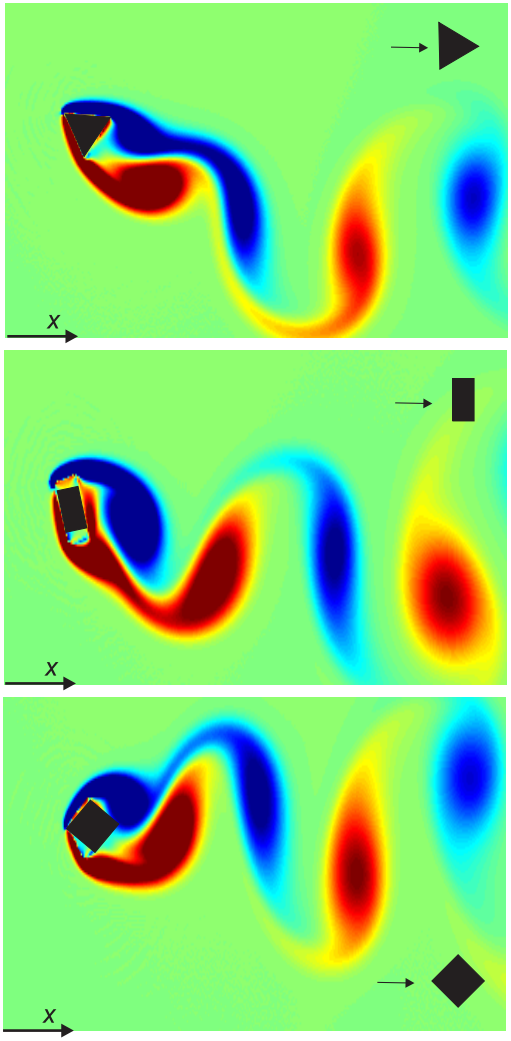


Figure 12. Vorticity contour with actuation ($K_1 = 1$) for a reduced velocity of $U^* = 4$, mass ratio m^* is 10, and damping parameter $\zeta = 0.04$ for equilateral triangle, rectangle (1:2 side), and 45º rhombi. It is shown the vorticity field when the body is at $Y = 0$ and going downwards.

4. Conclusions

The idea of imposing a rotation proportional to the motion-induced angle of attack on a galloping body has been studied, with its potential use for energy harvesting purposes in mind. A quasi-steady theoretical model to evaluate the dynamical behavior and the maximum efficiency of energy harvesting from Transverse Galloping with active pitch control has been developed and analyzed. The proposed model requires that the characteristic timescale of oscillation and rotation has to be much larger than the characteristic timescale of flow convection, which takes place usually under Transverse Galloping. In spite of the simplifications introduced in the model in order to arrive to analytical mathematical relationships (quasi-steady conditions, two term polynomial fitting of drag and lift coefficients, small motion-induced angle of attack, harmonic response), the present model is capable of correctly predicting the dynamics of oscillation as well as the energy harvested from the flow, with good agreement with computational results of the full fluid–solid interaction problem obtained through the Lattice Boltzmann Method. Note that the model may be useful as a design tool for practical implementations, for example to choose in advance the optimal rotating law (optimal K_1).

As a major result, it has been found that it is possible to increase importantly the efficiency of energy extraction (within the range of parameters tested), in particular, η_{max} has been increased up to three times with respect to the case without active rotation. Thanks to the pitch control law chosen, proportional to the motion-induced angle of attack and hence linked to the body's velocity, pitch variations are smooth and nearly sinusoidal (as the response of the body). To our knowledge, this type of active actuation linked to the body's dynamics response and with energy harvesting purposes is suggested here for the first time, and can be of interest from both the basic and the applied side. In addition, it should be noted that the proposed active actuation could be of interest to diminish Transverse Galloping response, to protect a structural element—for example, fixing a negative value of K_1; as K_1 becomes more negative, $\tilde{a_1}$ coefficient is diminished and galloping response is attenuated, in fact, for a high enough negative value of K_1, galloping is not possible. Finally, it should be noted that other rotating laws can be considered and should be evaluated.

Author Contributions: Conceptualization, A.B.-G.; Mathematical modelling, A.B.-G., D.G., F.S.; Numerical simulations, A.B.-G., D.V.-L. All authors have read and agreed to the published version of the manuscript.

Funding: This research received no external funding.

Conflicts of Interest: The authors declare no conflict of interest.

Appendix A. Numerical Simulation Method

The Lattice Boltzmann Method can be viewed as a discretized form of a finite velocity model of the Boltzmann Equation. Using the Bhatnar–Gross–Krook approximation, it follows [21]:

$$f_i(t+\delta_t, \mathbf{x}+\mathbf{e}_i\delta_t) = f_i(t,\mathbf{x}) + \frac{1}{\tau}\left(f_i^{eq}(t,\mathbf{x}) - f_i(t,\mathbf{x})\right), \tag{A1}$$

where $\mathbf{e}_i$ is the finite velocity set, $f_i(t,\mathbf{x})$ represents the mass density distribution of the particles moving in the $\mathbf{e}_i$ direction at time t and position $\mathbf{x}$, δ_t is the discrete time-step, τ is a relaxation time parameter, and f_i^{eq} is the equilibrium distribution given as

$$f_i^{eq} = w_i\rho\left(1 + \frac{\mathbf{e}_i\cdot\mathbf{u}}{c_s^2} + \frac{|\mathbf{e}_i\cdot\mathbf{u}|^2}{2c_s^4} - \frac{\mathbf{u}^2}{2c_s^2}\right), \tag{A2}$$

where w_i is a weighted parameter, ρ and $\mathbf{u}$ are, respectively, the macroscopic density and velocity of the fluid, and c_s the lattice sound speed. For our numerical simulations, it has been chosen to use the D2Q9 model, the discrete time-step δ_t is set equal to unity as well as the lattice spacing δ_x (then, $c_s = 1/\sqrt{3}$). Accordingly,

$$\mathbf{e}_i = \begin{cases} 0, & i = 0, \\ (\cos((i-1)\pi/4), \sin((i-1)\pi/4)), & i = 1-4, \\ \sqrt{(}2)(\cos((i-1)\pi/4), sin((i-1)\pi/4)), & i = 5-8, \end{cases} \tag{A3}$$

and the weighted parameter w_i is given as

$$w_i = \begin{cases} 4/9, & i = 0, \\ 1/9, & i = 1-4, \\ 1/36, & i = 5-8. \end{cases} \tag{A4}$$

The macroscopic variables such as the fluid density ρ and the fluid velocity $\mathbf{u}$ are related to f_i as

$$\rho = \textstyle\sum_i f_i, \quad \rho\mathbf{u} = \textstyle\sum_i \mathbf{e}_i f_i. \tag{A5}$$

The Lattice Boltzmann computer algorithm consists of two steps:

Collison: $\tilde{f}_i(t+1, \mathbf{x}) = f_i(t, \mathbf{x}) + \frac{1}{\tau}\left(f_i^{eq}(t, \mathbf{x}) - f_i(t, \mathbf{x})\right)$,
Streaming: $f_i(t+1, \mathbf{x} + \mathbf{e}_i) = \tilde{f}_i(t+1, \mathbf{x})$.

Applying the Chapman–Enskog expansion in the discrete Lattice Boltzmann Equation, the Navier–Stokes equations can be recovered for small Mach numbers. Then, the relaxation parameter can be related to the kinematic viscosity as

$$\nu = (2\tau - 1)/6. \tag{A6}$$

The viscosity has to be positive, so it requires $\tau > 0.5$; however, due to stability reasons, τ has to be higher than a certain threshold (see [22]), and, for the present article, τ has been fixed to 0.56. Regarding the Mach number, the computed numerical solutions are expected to converge towards an in-compressible limit when the fluid speed is sufficiently small compared with c_s , i.e., as the Mach number tends to zero. Thus, it has been chosen that the maximum local velocities cannot surpass 0.1 for any combination of the governing parameters.

Appendix A.1. Boundary Conditions

The left boundary is velocity specified inflow boundary condition with constant velocity profile U [23]. To simulate the in-compressible condition, the Mach number must be low enough. To this end, the inflow velocity U is set to 0.05. The rest of the boundaries are considered outflows with zero-extrapolation boundary [24]. For the boundary conditions of the cylinder, a no-slip boundary condition has been applied on the cylinder surface with an interpolated bounce-back scheme as developed by [22]:

$$\tilde{f}_{-i}(t, \mathbf{x}_b) = \tilde{f}_i(t, \mathbf{x}_f) - \chi\left(\tilde{f}_i(t, \mathbf{x}_f) - f_i^{eq}(t, \mathbf{x}_b)\right) + 3\omega_i\rho\mathbf{e}_{-i} \cdot \left(\mathbf{u}_{bf} - \mathbf{u}_f - 2\mathbf{u}_w\right), \tag{A7}$$

when $\Delta < 0.5$

$$\mathbf{u}_{bf} = \mathbf{u}_{ff}, \qquad \chi = (2\Delta - 1)/(\tau - 2), \tag{A8}$$

otherwise

$$\mathbf{u}_{bf} = (2\Delta - 3)\mathbf{u}_f/(2\Delta) + 3\mathbf{u}_{w/}(2\Delta), \qquad \chi = (2\Delta - 1)/(\tau + 0.5). \tag{A9}$$

Here, $\mathbf{x}_b$ is the position of the boundary node, $\mathbf{x}_w$ is the wall position and $\Delta = \|\mathbf{x}_f - \mathbf{x}_w\|/\|\mathbf{x}_f - \mathbf{x}_b\|$ is the distance to the wall from the fluid node and $\mathbf{u}_w$ the wall velocity.

As the cylinder moves, some lattice-points inside the cylinder become fluid nodes. In this case, the distribution function of any of these new fluid nodes is set equal to the equilibrium distribution with the cylinder's velocity and the density of the average value of neighboring fluid nodes.

Appendix A.2. Force Evaluation

Fluid force on the D-section cylinder has been calculated using the Momentum Exchange Algorithm (MEA) method [25] from the distribution function on the boundary directly. Then,

$$\mathbf{F} = \sum_{\mathbf{x}_b} \mathbf{e}_i (\tilde{f}_{-i}(t, \mathbf{x}_b) + \tilde{f}_i(t, \mathbf{x}_f)), \tag{A10}$$

where $\mathbf{x}_b$ are points of the boundary (D-section cylinder's surface, see Figure A1).

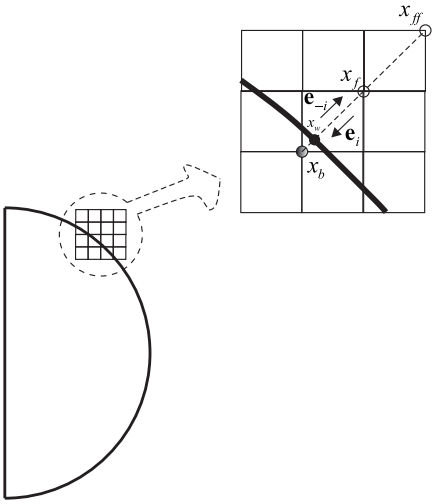


Figure A1. Schematics of the moving boundary condition treatment.

Appendix B. The Modeling of the Harvester as a Viscous Damper

An equivalent electrical circuit of an electromagnetic generator is shown in Figure A2. The induced voltage by velocity of oscillations $V_i = k_E \dot{y}$, current i, and the induced electromagnetic force F_{FEM} are described by the following equations:

$$k_E \dot{y} = (R_L + R_c) i + L \frac{di}{dt}, \qquad F_{FEM} = k_E i, \tag{A11}$$

where R_L is the resistance of the load connected to the generator, R_C is the internal resistance of the generator, L its inductance, and k_E is an electromechanical coupling constant determined by the flux density of the magnetic field and number of turns and length of the coil in the generator. When the inductance is negligible, it follows form Equation (A11) that

$$F_{FEM} = \frac{k_E^2}{R_L + R_C} \dot{y} = c\dot{y}, \tag{A12}$$

with $c = k_E^2/(R_L + R_C)$, which shows that the electromagnetic generator may be described as a pure viscous damper.

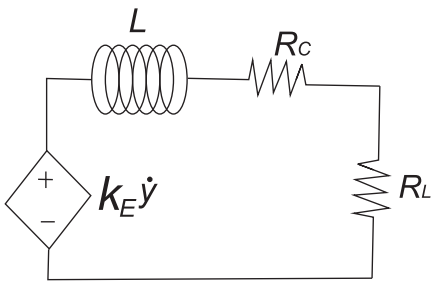


Figure A2. Equivalent electrical circuit of an electromagnetic generator.

Appendix C. The Mathematical Development to Arrive to Equations (16)

The dimensionless equation of the dynamics of the galloping body was (Equation (13)):

$$Y'' + 2\zeta Y' + Y = \frac{U^{*2}}{2m^*}\left(\tilde{a_1}\frac{Y'}{U^*} + \tilde{a_3}\frac{Y'^3}{U^{*3}}\right). \tag{A13}$$

Under sinusoidal oscillations of amplitude A^* and frequency ω^*, $Y = A^*\sin(\omega^*\tau)$, $Y' = A^*\omega^*\cos(\omega^*\tau)$, $Y'' = -A^*\omega^{*2}\sin(\omega^*\tau)$. Substituting Y, Y', and Y'' into Equation (A13) and equating sine and cosine terms, one finds that, for sine terms

$$-A^*\omega^{*2} + A^* = 0, \tag{A14}$$

and

$$2\zeta A^*\omega^* = \frac{U^{*2}}{2m^*}\left(\tilde{a_1}\frac{A^*\omega^*}{U^*} + \frac{3}{4}\tilde{a_3}\left(\frac{A^*\omega^*}{U^*}\right)^3\right), \tag{A15}$$

for cosine terms if $\cos(\omega^*\tau)^3$ is approximated by $3\cos(\omega^*\tau)/4$.

References

1. Bernitsas, M.M.; Raghavan, K.; Ben-Simon, Y.; Garcia, E.M.H. VIVACE (Vortex Induced Vibration Aquatic Clean Energy): A New Concept in Generation of Clean and Renewable Energy from Fluid. *J. Offshore Mech. Arct. Eng. ASME Trans.* **2006**, *130*, 041101. [CrossRef]
2. Bernitsas, M.M.; Ben-Simon, Y.; Raghavan, K.; Garcia, E.M.H. The VIVACE Converter: Model Tests at Reynolds Numbers Around 10^5. *J. Offshore Mech. Arct. Eng. ASME Trans.* **2006**, *131*, 1–13.
3. Barrero-Gil, A.; Sanz-Andres, A.; Alonso, G. Energy Harvesting from Transverse Galloping. *J. Sound Vib.* **2006**, *329*, 2873–2883. [CrossRef]
4. G.I.L.; A.B.; Lopez, A.G.V.; Prieto, J.R.A.; Acedo, Ó.P.; Ludlam, D.V.; Ji, X.U. Energy Converters and Energy Conversion Systems. U.S. Patent 9,541,058, 10 January 2017.
5. Sirohi, J.; Mahadik, R. Harvesting Wind Energy Using a Galloping Piezoelectric Beam. *J. Vib. Acoust.* **2010**, *134*, 011009. [CrossRef]
6. Sirohi, J.; Mahadik, R. Piezoelectric wind energy harvester for low-power sensors. *J. Intell. Mater. Syst. Struct.* **2011**, *22*, 2215–2228. [CrossRef]
7. Zhao, L.; Tang, L.; Yang, Y. Comparison of modeling methods and parametric study for a piezoelectric wind energy harvester. *Smart Mater. Struct.* **2013**, *22*, 125003. [CrossRef]
8. Yang, Y.; Zhao, L.; Tang, L. Comparative study of tip cross-sections for efficient galloping energy harvesting. *Appl. Phys. Lett.* **2013**, *102*, 064105. [CrossRef]
9. Xu-Xu, J.; Vicente-Ludlam, D.; Barrero-Gil, A. Theoretical study of the energy harvesting of a cantilever with attached prism under aeroelastic galloping. *Eur. J. Mech.* **2016**, *60*, 189–195. [CrossRef]
10. Blevins, R. *Flow-Induced Vibrations, Van Nostrand Reinhold*; Van Nostrand Reinhold Company: New York, NY, USA, 1990.
11. Naudascher, E.; Rockwell, D. *Flow-Induced Vibrations: An Engineering Guide*; A.A. Balkema, Rotterdam: Avereest, The Netherlands, 1994.
12. Païdoussis, M.P.; Price, S.J.; De Langre, E. *Fluid-Structure Interactions: Cross-Flow-Induced Instabilities*; Cambridge University Press: Cambridge, UK, 2011.
13. Abdelkefi, A.; Yan, Z.; Hajj, M.R. Performance analysis of galloping-based piezoaeroelastic energy harvesters with different cross-section geometries. *J. Intell. Mater. Syst. Struct.* **2014**, *25*, 246–256. [CrossRef]
14. Vicente-Ludlam, D.; Barrero-Gil, A.; Velazquez, A. Enhanced mechanical energy extraction from transverse galloping using a dual mass system. *J. Sound Vib.* **2015**, *339*, 290–303. [CrossRef]
15. Vicente-Ludlam, D.; Barrero-Gil, A.; Velazquez, A. Optimal electromagnetic energy extraction from transverse galloping. *J. Fluids Struct.* **2014**, *51*, 281–291. [CrossRef]

16. Abdelmoula, H.; Abdelkefi, A. Piezoaeroelastic investigation on the control and energy harvesting of galloping systems. In Proceedings of the 57th AIAA/ASCE/AHS/ASC Structures, Structural Dynamics, and Materials Conference, San Diego, CA, USA, 4–8 January 2016.
17. Rizzoni, G.; Hartley, T.T. *Principles and Applications of Electrical Engineering*; Mc-Graw Hill: New York, NY, USA, 2000.
18. Vicente-Ludlam, D.; Barrero-Gil, A.; Velazquez, A. Flow-induced vibration of a rotating circular cylinder using position and velocity feedback. *J. Fluids Struct.* **2017**, *72*, 127–151. [CrossRef]
19. Sorribes-Palmer, F.; Sanz-, res, A. Optimization of energy extraction in transverse galloping. *J. Fluids Struct.* **2013**, *43*, 124–144. [CrossRef]
20. Bhinder, A.; Sarkar, S.; Dalal, A. Flow over and forced convection heat transfer around a semi-circular cylinder at incidence. *Int. J. Heat Mass Transf.* **2012**, *55*, 5171–5184. [CrossRef]
21. Higuera, F.J. Boltzmann approach to lattice gas simulations. *EPL (Europhys. Lett.)* **1989**, *9*, 663. [CrossRef]
22. Mei, R.; Luo, L.S.; Shy, W. An accurate curved boundary treatment in the lattice Boltzmann method. *J. Comput. Phys.* **1999**, *155*, 307–330. [CrossRef]
23. Zhou, Q.; He, X. On pressure and velocity boundary conditions for the lattice Boltzmann BGK model. *Phys. Fluids* **1997**, *9*, 1591–1598. [CrossRef]
24. Yu, D.; Mei, R.; Luo, L.S.; Shy, W. Viscous flow computations with the method of lattice Boltzmann equation. *Progress Aerosp. Sci.* **2003**, *39*, 329–367. [CrossRef]
25. Caiazzo, A.; Junk, M. Boundary forces in lattice Boltzmann: Analysis of momentum exchange algorithm. *Comput. Math. Appl.* **2008**, *55*, 1415–1423. [CrossRef]



© 2020 by the authors. Licensee MDPI, Basel, Switzerland. This article is an open access article distributed under the terms and conditions of the Creative Commons Attribution (CC BY) license (http://creativecommons.org/licenses/by/4.0/).